Chin. J. Geochem.
DOI 10.1007/s11631-015-0051-9

ORIGINAL ARTICLE

Sulfur determination by laser ablation high resolution magnetic sector ICP-MS applied to glasses, aphyric lavas, and micro-laminated sediments

Xu-Jie Shu[1,2] · **Cin-Ty A. Lee**[1]

Received: 1 December 2014 / Revised: 25 March 2015 / Accepted: 29 March 2015

Abstract Sulfur (S) is an important element for understanding redox processes, ore formation, environmental chemistry, volcanism and climate. Here, we present a method for in situ S concentration measurement by LA-ICP-MS at the 50–100 μm length scale using a 213 nm laser ablation set up coupled to a single-collector magnetic sector ICP-MS with high resolution capabilities. Analyses were performed in medium mass resolution ($m/\Delta m = 3000$) mode, which allows for the separation of ^{32}S and ^{34}S from molecular interferences. S is simultaneously analyzed along with all major and minor elements so that a priori knowledge of an internal standard concentration is not necessary; this allows for in situ bulk analysis of aphyric groundmass in volcanic rocks or other fine-grained samples. The primary limitation in analyzing S by laser ablation was found to be long-term instrumental drift in fractionation of elemental S relative to other elements, presumably due to drift in laser dynamics. A method for correcting for such fractionation over time was implemented. After correcting for such drift, measurements of homogeneous basaltic glasses are reproducible to within 10 % for high concentration samples (>500 ppm) and to within 20 % for low concentration samples (<200 ppm). The applicability of the method was demonstrated using natural and synthetic glasses, aphyric lavas, and micro-laminated sediments.

Keywords Sulfur · Icp-ms · Glass

✉ Cin-Ty A. Lee
ctlee@rice.edu

[1] Department of Earth Science, MS-126, Rice University, 6100 Main Street, Houston, TX 77005, USA

[2] State Key Laboratory for Mineral Deposits Research, School of Earth Science and Engineering, Nanjing University, Nanjing 210093, China

1 Introduction

In this paper, we outline a method for in situ bulk measurement of S at the 50–100 μm lengthscale by laser ablation inductively coupled plasma mass spectrometry (LA-ICP-MS). We also develop new glass reference materials and provide new concentration measurements of existing reference materials, calibrated against gravimetric S standards determined by solution ICP-MS (Erdman et al. 2013). Our interest in in situ bulk measurements by LA-ICP-MS is motivated by the importance of S to redox, ore deposits, environmental chemistry, volcanic gases, and climate (Alt 1995; Alt et al. 2012, 1993; Burgisser and Scaillet 2007; De Hoog et al. 2004, 2001; Jego and Dasgupta 2013; Jugo 2009; Lee et al. 2012; Mavrogenes and O'Neill 1999; Metrich and Mandeville 2010; O'Neill and Mavrogenes 2002; Self et al. 2008; Wallace 2005; Wallace and Edmonds 2011). Whole-rock analysis of S is well-established using combustion, titration or dissolution of rock powders, followed by analysis using spectrophotometers or mass spectrometers. Sample masses as low as 30 mg can now be analyzed by these whole-rock methods. For a nominal density of $\sim$2.7 g/cm^3, this means that whole-rock analyses (via microdrilling) could in theory provide S concentration determinations at the 3–4 mm lengthscale or larger. In cases where the sample is smaller, such as in the case of melt inclusions, or when one desires to avoid the effects of alteration, in situ determination may be necessary. The best established techniques for in situ determination of S are secondary ion mass spectrometry (SIMS) and electron probe micro-analysis (EPMA). These methods require homogeneous samples at the <20 μm scale and have become the standard method for measuring the S content of volcanic glasses, particularly melt inclusions hosted within phenocrysts. There is, however, a need

Published online: 16 April 2015

for measurements at intermediate lengthscales because many samples of interest (authigenic materials, sediments, and the majority of aphyric volcanic rocks) are heterogeneous on the tens of microns lengthscale.

Laser ablation inductively coupled plasma mass spectrometry (LA-ICP-MS) offers the potential for measuring S contents at lengthscales of 20–100 μm and is well-established as a sensitive and rapid analytical method for in situ measurement of trace elements in geological materials (Lee et al. 2009; Liu et al. 2008; Longerich et al. 1996). Rare earth elements, large ion lithophile elements, high field strength elements, and first row transition metals are convention. Measurement of S concentration by LA-ICP-MS, however, has not been fully developed. The main limitations in measuring S concentration by LA-ICP-MS are the availability of well-characterized standards, molecular interferences on all the S masses, and instrumental drift (Ripley et al. 2011). In particular, because laser ablation is destructive, existing S reference materials, such as mid-ocean ridge basalt (MORB) glasses, are in dwindling supply. This paper discusses these complications and how we overcome them.

2 Analytical methods

The primary focus of this study was to measure major and trace elements concentrations in situ by LA-ICP-MS at Rice University. We used a New Wave 213 nm laser ablation system coupled to a Thermo-Finnigan Element 2 magnetic-sector ICP-MS. Ablation was performed with a circular spot size of 110 μm in diameter, 15 J/cm^2 fluence, and a repetition rate of 10 Hz. The ablated material was carried out of the ablation cell with He gas (850 mL/min) and then mixed with Ar gas before entering the ICP-MS (cool gas of 13.33, auxiliary gas of 0.95 and sample gas of 0.8 L/min). Sensitivity in low mass resolution (m/Δm ~300) was ~30,000 cps per ppm of La for a spot size of 55 μm. Sensitivity in medium mass resolution (m/Δm ~3000) was ~3000 cps per ppm of La for a spot size of 55 μm. In order to resolve ^{32}S, ^{33}S, and ^{34}S from molecular intereferences, measurements were made in medium mass resolution mode (m/Δm = 3000). This mass resolution is sufficient enough to separate ^{32}S, ^{33}S, and ^{34}S from the dominant molecular interferences $^{16}O^{16}O^+$, $^{16}O^{17}O^+$, and $^{16}O^{18}O^+$ (Fig. 1). Sensitivity for sulfur in medium mass resolution was 1000 cps/ppm for 55 μm diameter spot size, 15 J/cm^2 fluence, and a repetition rate of 10 Hz. The following masses were analyzed in our general protocol: ^{23}Na, ^{25}Mg, ^{27}Al, ^{30}Si, ^{31}P, ^{32}S, ^{33}S, ^{34}S, ^{39}K, ^{43}Ca, ^{45}Sc, ^{48}Ti, ^{49}Ti, ^{51}V, ^{52}Cr, ^{55}Mn, ^{57}Fe, ^{59}Co, ^{60}Ni, ^{63}Cu, ^{66}Zn, ^{69}Ga, ^{73}Ge, ^{74}Ge, ^{89}Y, ^{91}Zr. Because we analyzed in medium mass resolution where sensitivities are lower, all signal sizes were within the linear range of the detector. In addition, the concentrations of elements in our external standards were

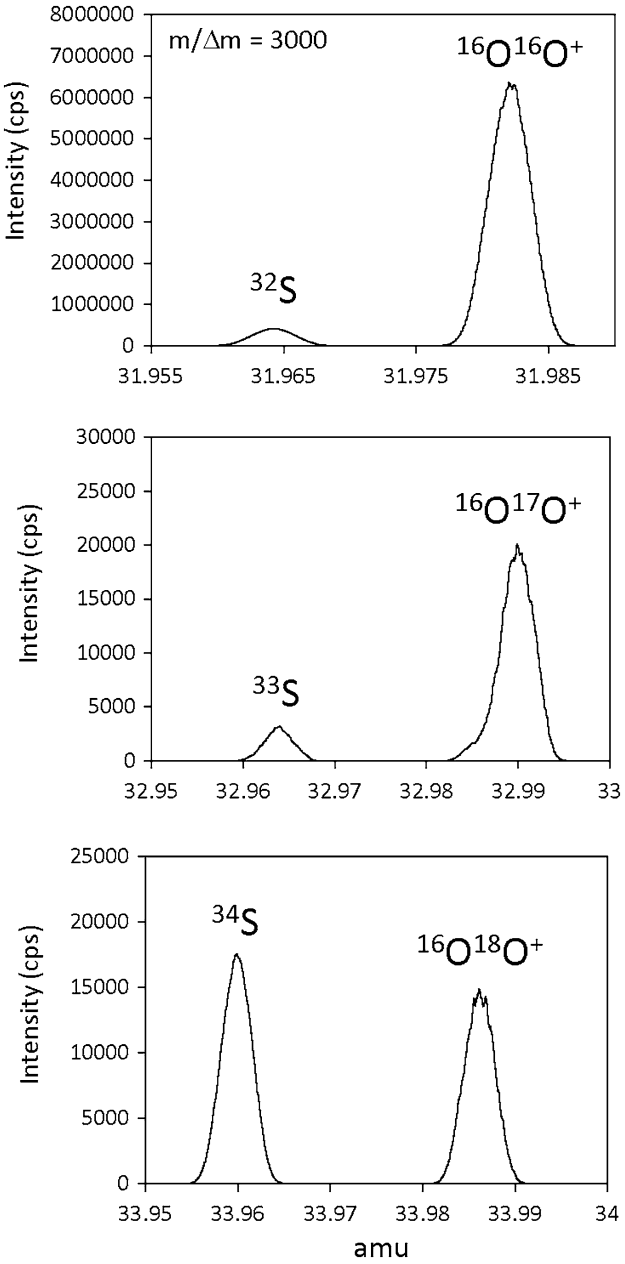

Fig. 1 Mass scans of S isotopes and nearby molecular interferences in medium mass resolution mode (m/Δm = 3000). Note that in these scans, no attempt was made to refine the mass calibration of the magnet, so measured mass does not correspond exactly to the actual mass of a particular nuclide

similar to the concentrations in the samples to within an order of magnitude, so no corrections for non-linearity were needed. Mass spectrometry protocols were as follows: 8 samples per peak, 0.001 s sampling time (in E-scan), 0.03 s magnetic settling time, and 100 % mass window. The time for one cycle was 3.5 s, and a total of 50 cycles, including 10 cycles with the laser off, were measured. Long term drift of mass calibration was corrected for in real time by monitoring the mass offset of the $^{40}Ar^{40}Ar^+$ dimer before every

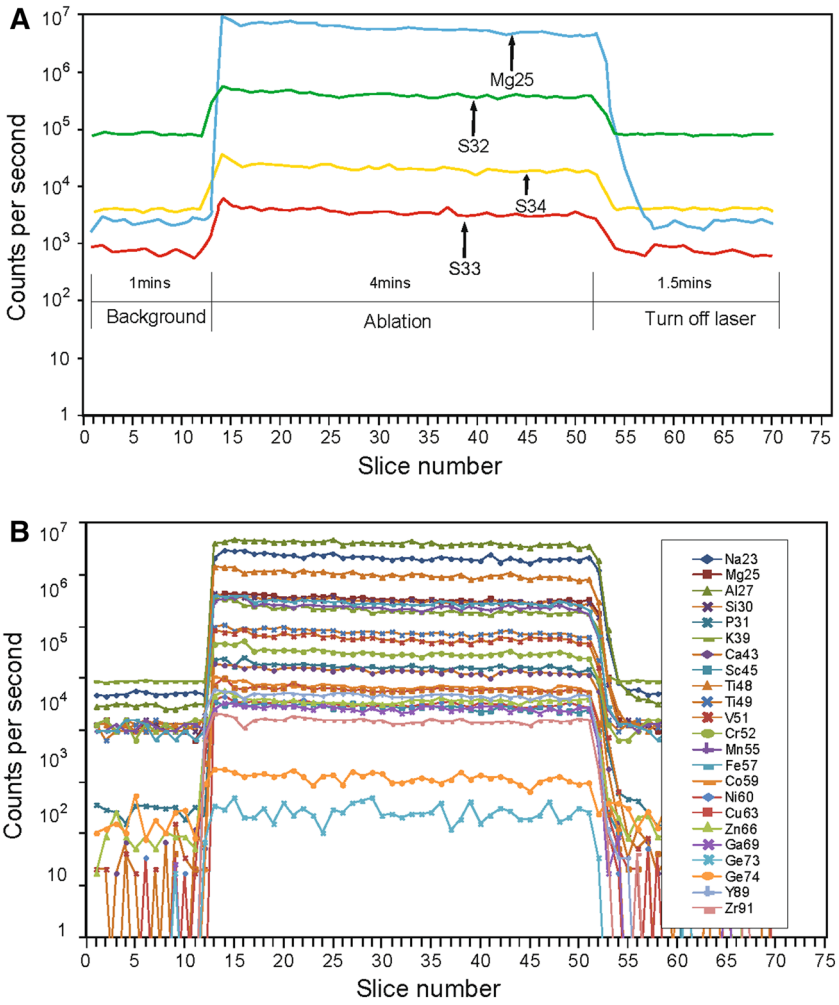

Fig. 2 Example of a time-resolved signal for laser ablation inductively coupled plasma mass spectrometry (LA-ICP-MS), including background and sample analysis

measurement and correcting the total mass calibration accordingly. Small systematic deviations from the mass calibration were corrected for by calculating the mass offset of the peak relative to the actual mass of the isotope of interest. Laser ablation analyses were done in time-resolved mode (Fig. 2), beginning with a ~30 s background acquisition (laser off), followed by a 3–4 min ablation interval, and ending with another ~30 s background acquisition. Reference glass standards were run before and after each sequence of samples (approximately every 2 h). Most measurements represent spot analyses. When line scans were performed, a scan speed of 15 μm/s was adopted.

3 External standards and samples

Samples utilized in this study include both synthetic and natural glasses. These include synthetic United States Geological Survey Hawaiian basalt glass (BHVO-2g) and Columbia River basalt glass (BCR-2g), mid-ocean ridge basalt (MORB) glasses from the Smithsonian Museum collection (Melson et al. 2002), natural rhyolitic obsidian glasses M3-86, M3-79 and M3-33 from the Oregon Cascades (Savov et al. 2009), synthetic S-bearing colored glasses manufactured by Bullseye Glass (001322-0003-F-P001 and 000203-0003-F-P005; www.bullseyeglass.com) and synthetic S-bearing amber-colored glass from a Bud Light™ beer bottle (Anheuser-Busch) and a Saint Arnold's beer bottle (a local Texas brewery). BHVO-2g, BCR-2g were used simultaneously as external standards for all elements (Gao et al. 2002) except for S.

We used established MORB glasses as external standards for S. Reported concentrations of S by EPMA, SIMS or LA-ICP-MS for VG2 (from Juan de Fuca ridge, Jarosewich et al. 1979; Thornber et al. 2002) are shown in Table 1: 1403 ± 31 ppm (1 SD for all the errors, O'Neill and Mavrogenes 2002), 1340 ± 80 ppm (Dixon et al. 1991), 1420 ± 40 ppm (Wallace and Carmichael 1992),

Table 1 Published S concentrations of MORB glass standards

VG2 ppm	SD	A99 ppm	SD	Reference	Methods
1403	31			O'Neill and Mavrogenes (2002)	Electron Microprobe
1340	80	170	30	Dixon et al. (1991)	Electron Microprobe
1420	40			Wallace and Carmichael (1992)	Electron Microprobe
1400				Nilsson and Peach (1993)	Electron Microprobe
1365	29	135	50	Thordarson et al. (1996)	Ion probe
		200	50	Thordarson et al. (1996)	LA-ICP-MS
1450	30			Metrich et al. (1999)	Electron Microprobe
1416	36	177	21	De Hoog et al. (2001)	Electron Microprobe
1300	44	155	9	Bell et al. (2009)	Electron Microprobe
1305	135	96	63	Thornber et al. (2002)	Electron Microprobe
1378	53	156	37	Average	

1400 ppm (Nilsson and Peach 1993), 1365 ± 29 ppm (Thordarson et al. 1996), 1450 ± 30 ppm (Metrich et al. 1999), 1416 ± 36 ppm (De Hoog et al. 2001), and 1300 ± 44 (Bell et al. 2009). Reported values for A99 are 177 ± 21 ppm (De Hoog et al. 2001), 135 ± 50 ppm (Cameca trace routine), 200 ± 50 ppm (CSIRO trace routine; Thordarson et al. 1996), 170 ± 30 ppm (Dixon et al. 1991), and 155 ± 9 ppm (Bell et al. 2009). It can be seen that interlaboratory values for VG2 vary by ~11 % (1300–1450 ppm) and those for A99 by ~48 % (135–200 ppm). The higher variability for A99 is almost certainly due to difficulties in measuring S at such low abundances. In this study, we use VG2 as an external S standard.

4 Data reduction

4.1 Internal and external calibration

Sample signal intensities were converted to concentrations using a combination of external and internal standards following the basic principles outlined in Longerich et al. (1996). For external calibration, we used VG2 for S and USGS BHVO-2g and BCR-2g for all other elements (Gao et al. 2002). To correct for slight variations in ablation efficiency between samples and external standards, an internal standard was monitored. In general, the internal standard is usually chosen to be an element that occurs in sufficient quantity in all samples and standards and whose concentration is known independently. However, in the case of sample unknowns, prior knowledge of the concentration of an internal standard is not necessary if all major and minor elements are analyzed, as shown below (Lee et al. 2008; Liu et al. 2008).

Data reduction proceeded as follows. We first averaged the pre-ablation background signal for each element. This background signal was then subtracted from every ablation signal to obtain a background-corrected signal, which is the quantity we refer to from here on. To convert sample signal intensity (cps) to concentration (ppm) for an element i, e.g., C_i^{Sa}, the following equation was used

$$C_i^{Sa} = \left(\frac{I_i^{Sa}}{I_{is}^{Sa}}\right)\left(\frac{C_i^R/C_{is}^R}{I_i^R/I_{is}^R}\right)C_{is}^{Sa} \quad (1)$$

The first parenthesized quantity corresponds to the measured background-corrected signal of an element i in the sample (I_i^{Sa}) normalized to the signal of the internal standard is in the sample (I_{is}^{Sa}). The second parenthesized quantity essentially represents the external calibration, wherein C_i^R/C_{is}^R is the concentration ratio of element i to the internal standard in the external standard and I_i^R/I_{is}^R is the signal ratio of element i to the internal standard signal in the external standard. When using more than one external standard for calibration, the second parenthesized quantity represents the slope of the concentration versus signal intensity calibration curve. Finally, the last quantity on the right is C_{is}^{Sa} is the concentration of an internal standard in the sample. The internal standard concentration in the sample and the external calibration factor must be known to convert sample intensities into concentrations.

Determining the concentration of the internal standard in a sample was done by analyzing all major and minor cations and assuming their oxides sum to 100 %. We measured Na, K, Ca, Mg, Al, Si, P, Mn, Fe and Ti and assumed their oxides correspond to K_2O, CaO, MgO, Al_2O_3, SiO_2, P_2O_5, MnO, FeO and TiO_2. All Fe was taken to be in the +2 valence state, so an uncertainty is introduced if some fraction of the total Fe is Fe^{3+}. Because we do not measure H_2O or other volatiles, concentrations are thus estimated on

a volatile-free basis. The assumption here is that S is not a major element because we are interested primarily in silicates. Signal intensities for a given element were converted to effective oxide intensities by (1) dividing by the isotopic abundance fraction of the monitored isotope, (2) dividing by the number of cations per oxide formula unit (e.g., to convert Al to Al_2O_3, divide by 2 Al/Al_2O_3) and (3) multiplying by the molecular weight of the oxide. Then the following algorithm was performed. The assumption that all major and minor oxides were determined gives $\sum_i X_i^{Sa} = 1$, where X_i^{Sa} is the oxide weight fraction of element i and the summation is over all oxides. Dividing by a reference cation, X_{is}^{Sa}, which we take here to be our internal standard and re-arranging yields

$$X_{is}^{Sa} = \left(1 + \sum_{i,i\neq is} X_i^{Sa}/X_{is}^{Sa}\right)^{-1} \quad (2)$$

The oxide weight fraction ratios are calibrated against external standards using Eq. 1 after converting elemental signal intensities to effective oxide signal intensities as described above:

$$\frac{X_i^{Sa}}{X_{is}^{Sa}} = \left(\frac{I_i^{Sa}}{I_{is}^{Sa}}\right)\left(\frac{X_i^R/X_{is}^R}{I_i^R/I_{is}^R}\right) \quad (3)$$

Equation 3 is then plugged into Eq. 2 to obtain X_{is}^{Sa}. Then Eq. 1 is used to determine absolute concentrations of all oxides and elements. While the above equations are designed for the analysis of trace S in silicate materials, it is trivial, with a little thought, to modify the above equations to accommodate materials, such as sulfides and sulfates, in which S is a major element.

4.2 Long-term drift in elemental fractionations

An implicit assumption of reducing LA-ICP-MS data is that relative sensitivity between elements does not change, even if the absolute sensitivity of the instrument drifts with time or between samples. However, in our study, we found that measured elemental ratios drift with time, especially the ratio of S with respect to other elements. For example, raw S/Mg signal ratios drift by 15 % over the course of 5 h, whereas ratios of other elements relative to Mg drifted by no more than 5 %. Presumably, the effect on S is more pronounced because S is volatile, but we do not see any drift in S/Mg signal during a single analysis, that is, there is no downhole elemental fractionation. We find that these long-term drifts do not appear to be related to changes in the gas background associated with accumulation of materials on the side walls of the tubing or ablation cell because we observe no change in gas background signal during the day or from day to day. More likely, the long-term drifts in elemental fractionation, especially that of S, are probably related to long-term drifts in gas flow dynamics of the ablation cell or laser fluence, although we cannot be certain.

What is important is that S/Mg fractionation factors drifts linearly on long timescales (>1 h) so that regardless of what is causing the drift, a drift correction can be made. In Fig. 3, we show that S/Mg signal ratios drift for all samples. In particular, we show that all samples display the same relative rate of drift to within error, regardless of S concentration. For example, VG2 and MORB 2380-12 have S concentrations >1000 ppm and BHVO-2G, BCR-2G and A99 <300 ppm S, but they exhibit the same relative drift in S/Mg intensity ratios. These observations indicate that the relative rate of drift is not dependent on S concentration, matrix effects, or accumulated memory effects. To correct for drift in elemental fractionation, we adopt the following protocol, which we applied to S and all other elements. We define the relative rate of change of an elemental ratio D as

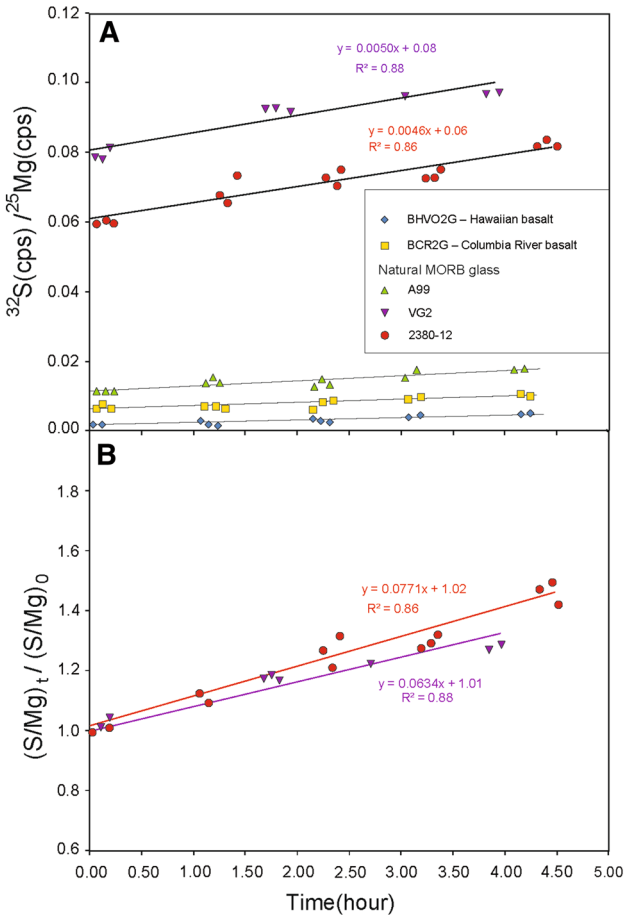

Fig. 3 Elemental fractionation drift with time. **a** Change of $^{32}S/^{25}Mg$ background-corrected signal ratios (cps/cps) over time, which shows a linear increase in $^{32}S/^{25}Mg$ ratio with time. **b** Change of $^{32}S/^{25}Mg$ normalized to initial $^{32}S/^{25}Mg$ showing that relative drift is constant regardless of S concentration and S/Mg ratio

$$D \equiv \left(\frac{\left(I_i^R/I_{is}^R\right)_t - \left(I_i^R/I_{is}^R\right)_o}{T_t - T_o} \right) \left(\frac{I_{is}^R}{I_i^R} \right)_o \quad (4)$$

T_o is the clock time at which a given sample was initially measured and T_t is the clock time at which the same sample was later measured. Ideally, the difference in time between the two measurements ($T_t - T_o$) should be long enough to bracket an interval over which a number of samples were measured, but not so long that the relative drift rate has changed. For our studies, the appropriate time difference was ~2–3 h. The other symbols in Eq. 4 represent the signal ratios measured at time T_t and T_o. D can be determined by measuring the same sample at the beginning and end of an analysis period. In practice, D is determined by measuring many different samples and then averaged to generate a universal D. Because Eq. 4 does not require knowledge of absolute concentrations, D can be determined from external standards as well as sample unknowns, although materials with high S content (>800 ppm) are preferable so as to establish a statistically significant D.

Once D is estimated, the value can be applied to all other samples to obtain a drift-corrected signal ratio $\left(I_i^{Sa}/I_{is}^{Sa}\right)_{corr}$:

$$\left(\frac{I_i^{Sa}}{I_{is}^{Sa}} \right)_{corr} = \frac{\left(I_i^{Sa}/I_{is}^{Sa}\right)_t}{1 + (T_t - T_o)D} \quad (5)$$

where $\left(I_i^{Sa}/I_{is}^{Sa}\right)_t$ is the background-corrected signal ratio in the sample measured at time T_t and T_o is now a common reference clock time, e.g., the time of the measurement of the day. Figure 4 shows how calibration curves compare before and after elemental fractionation drift corrections are applied. We note that should there be matrix effects, the drift correction can be done by measuring the same sample in the beginning and at the end of the acquisition.

4.3 Limit of detection and precision

Limit of detection (LOD) is the minimum signal that can be resolved from the background. We define the LOD as three times the standard deviation of the background signal $3\sigma^{back}$, normalized to the sensitivity of the instrument during each measurement. This is given by

$$\frac{LOD_i^{Sa}}{C_{IS}^{Sa}} = \frac{3 \times \sigma_i^{back}}{\bar{I}_{IS}^{Sa}} \times \frac{C_i^R}{C_{IS}^R} \times \frac{I_{IS}^R}{I_i^R} \quad (6)$$

Internal precision (in-run precision) is defined by the standard deviation of the ratio of a given signal normalized to the signal of the internal standard mass. External precision for individual spot measurement is quantified by multiple analyses on the same sample, assuming the sample is homogeneous.

5 Results

5.1 Data quality and standardization using VG2

We measured ^{32}S, ^{33}S and ^{34}S, but the signal to background ratio of ^{33}S was too low to evaluate, owing to its low isotopic abundance. The LOD for a 110 μm diameter spot

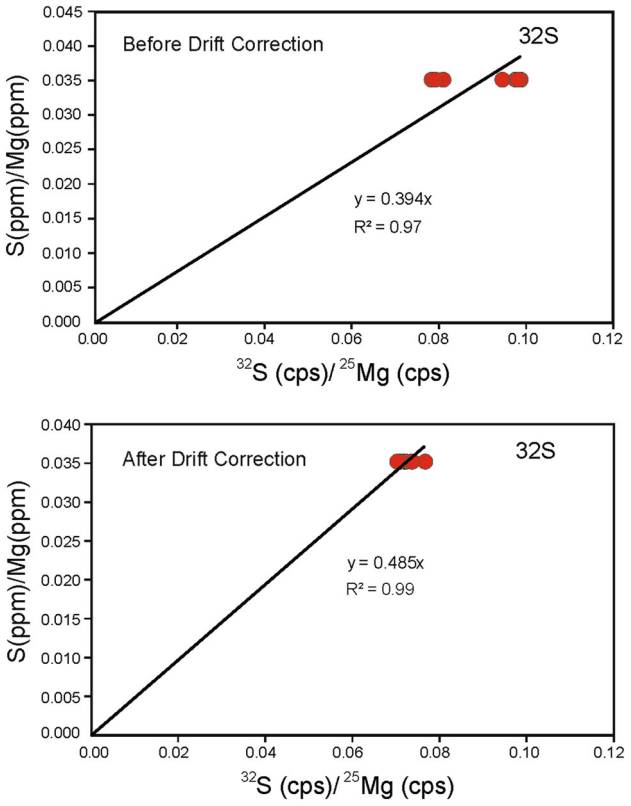

Fig. 4 External standard calibration of $^{32}S/^{25}Mg$ before and after correction for drift in elemental fractionation

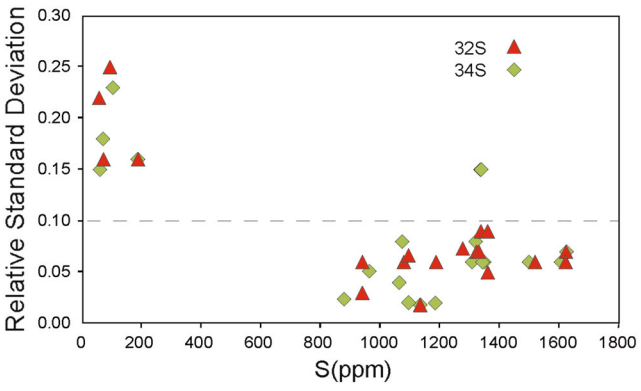

Fig. 5 External reproducibility (1 SD) as a function of S concentration

Table 2 Volcanic glasses

n	Mid Ocean Ridge Basalt													
	A99		VG		6170		6171		6172		6190		6191	
	69		14		4		4		6		5		6	
	Ave	SD	Ave	SD	Ave	SD	Ave	SD	Ave	SD	Ave	SD	Ave	SD
SiO_2 (wt%)	50.24	1.64	47.63	2.81	50.84	1.21	51.39	0.71	50.41	0.70	50.55	1.07	50.65	0.99
TiO_2 (wt%)	2.85	1.77	1.31	0.06	1.64	0.06	1.75	0.10	1.32	0.03	1.70	0.12	1.89	0.06
Al_2O_3 (wt%)	12.73	1.13	15.59	2.44	15.82	0.29	14.74	0.48	14.38	0.50	13.88	0.90	12.65	1.04
MgO (wt%)	5.04	0.35	8.06	0.48	7.52	0.18	6.89	0.55	7.83	0.42	6.62	0.52	5.98	0.19
FeO (wt%)	12.96	0.60	8.70	0.75	8.49	8.20	0.17	0.67	9.19	0.16	9.57	0.82	11.16	1.00
MnO (wt%)	0.19	0.01	0.17	0.02	0.16	0.01	0.16	0.01	0.17	0.01	0.18	0.02	0.20	0.01
CaO (wt%)	9.34	0.49	11.79	1.28	8.77	0.46	9.09	0.31	11.36	0.48	10.48	0.32	10.03	0.32
Na_2O (wt%)	2.67	0.18	2.42	0.27	4.11	0.18	3.88	0.27	2.55	0.14	2.80	0.13	2.82	0.16
K_2O (wt%)	0.80	0.08	0.07	0.01	0.19	0.01	0.23	0.03	0.12	0.01	0.20	0.02	0.17	0.01
P_2O_5 (wt%)	0.44	0.04	0.11	0.02	0.20	0.07	0.26	0.02	0.14	0.00	0.20	0.02	0.18	0.02
Sc (ppm)	32.6	3.5	42.4	11.4	27.4	1.2	30.6	0.8	35.4	1.7	37.9	5.1	41.6	4.4
V (ppm)	373	29	237	37	241	7	257	33	287	12	294	32	349	33
Cr (ppm)	36	4	238	42	267	17	184	36	357	33	249	27	96	11
Co (ppm)	40	3	36	5	35	1	36	1	40	1	35	4	39	4
Ni (ppm)	44	4	104	18	131	5	90	37	102	9	79	9	43	5
Cu (ppm)	208	13	52	4	58	2	54	1	77	2	62	4	55	3
Zn (ppm)	112	22	49	19	60	2	68	9	66	3	60	10	72	17
Ga (ppm)	24	2	14	2	15	0	17	1	16	1	16	1	17	2
Ge (ppm)	1.5	0.1	1.2	0.2	1.4	0.1	1.5	0.1	1.4	0.1	1.4	0.1	1.4	0.1
Y (ppm)	41	6	40	15	28	1	33	2	27	2	33	5	42	8
Zr (ppm)	275	34	98	30	150	9	150	6	81	7	128	15	126	16
S (^{32}S) (ppm)	187	29	1078	64	943	33	1138	20	1076	61	1336	119	1518	89
S (^{34}S) (ppm)	181	30	1072	82	869	25	1029	36	1062	41	1307	72	1498	93

n	Mid Ocean Ridge Basalt															
	6192		6193		6194		6195		6196		6197		6198		6199	
	7		4		6		6		5		7		6		6	
	Ave	SD	Ave	SD	Ave	SD	Ave	SD	Ave	SD	Ave	SD	Ave	SD	Ave	SD
SiO_2 (wt%)	51.11	1.80	49.88	0.47	50.31	1.32	49.13	1.90	49.86	1.68	48.60	2.84	48.41	1.22	49.52	1.47
TiO_2 (wt%)	1.40	0.07	1.48	0.15	1.86	0.27	1.87	0.09	1.83	0.08	1.71	0.11	1.87	0.14	0.67	0.52
Al_2O_3 (wt%)	14.14	0.99	14.57	0.57	13.97	2.24	12.81	0.83	13.03	0.75	14.59	2.29	14.78	0.95	13.63	1.03
MgO (wt%)	7.24	0.20	7.08	0.71	6.43	0.97	6.58	0.29	6.54	0.27	7.18	0.63	6.93	0.39	7.89	0.39
FeO (wt%)	8.55	0.66	8.53	0.94	10.51	0.84	11.65	0.62	11.15	0.96	9.38	1.24	9.76	0.71	9.33	0.98
MnO (wt%)	0.16	0.01	0.16	0.01	0.19	0.01	0.21	0.01	0.21	0.01	0.18	0.02	0.18	0.01	0.18	0.01
CaO (wt%)	10.12	0.52	10.80	0.41	10.01	0.69	10.85	0.40	10.92	0.54	11.12	0.90	10.71	0.34	12.26	0.50
Na_2O (wt%)	2.84	0.18	2.78	0.25	2.91	0.30	2.42	0.12	2.36	0.20	2.71	0.34	2.97	0.22	2.17	0.15
K_2O (wt%)	0.17	0.02	0.11	0.01	0.14	0.02	0.13	0.01	0.13	0.02	0.12	0.02	0.14	0.01	0.03	0.00
P_2O_5 (wt%)	0.15	0.02	0.13	0.01	0.16	0.03	0.17	0.01	0.16	0.02	0.16	0.03	0.18	0.02	0.06	0.01
Sc (ppm)	35.7	3.6	40.2	5.4	40.7	5.9	45.5	5.6	46.7	6.1	44.8	11.1	42.2	5.6	45.5	5.9
V (ppm)	248	28	252	28	290	32	348	35	346	35	267	48	282	28	255	30
Cr (ppm)	251	34	272	36	153	80	121	14	124	17	238	68	221	22	192	24
Co (ppm)	35	3	34	4	37	3	40	4	39	4	35	4	36	3	42	5
Ni (ppm)	100	8	74	10	60	22	43	4	44	5	70	18	71	10	48	7
Cu (ppm)	64	6	70	9	65	8	56	4	56	3	65	10	62	4	85	8

Table 2 continued

n	Mid Ocean Ridge Basalt															
	6192		6193		6194		6195		6196		6197		6198		6199	
	7		4		6		6		5		7		6		6	
	Ave	SD	Ave	SD	Ave	SD	Ave	SD	Ave	SD	Ave	SD	Ave	SD	Ave	SD
Zn (ppm)	53	11	50	14	67	15	70	16	67	17	53	19	59	15	51	15
Ga (ppm)	15	2	15	2	17	2	17	1	16	2	15	2	17	2	14	2
Ge (ppm)	1.7	0.9	1.4	0.2	1.4	0.1	1.4	0.1	1.4	0.2	1.3	0.2	1.4	0.1	1.3	0.2
Y (ppm)	26	13	36	7	42	11	44	8	45	9	43	16	45	9	28	6
Zr (ppm)	96	16	109	18	119	23	121	19	120	19	138	42	143	24	49	8
S (^{32}S) (ppm)	1091	74	1186	71	1359	124	1621	113	1620	90	1273	96	1329	96	1359	72
S (^{34}S) (ppm)	1098	23	1183	20	1372	179	1623	110	1605	101	1308	93	1348	79	1342	84

n	Mid Ocean Ridge Basalt				Rhyolite						USGS Synthetic Glasses			
	F31		2380-12		M3-33		M3-79		M3-86		BHVO2g		BCR2g	
	4		94		10		10		10		85		81	
	Ave	SD	Ave	SD	Ave	SD	Ave	SD	Ave	SD	Ave	SD	Ave	SD
SiO_2 (wt%)	46.60	2.93	49.05	1.54	77.05	1.22	75.27	0.96	76.41	0.46	49.36	1.91	54.32	1.41
TiO_2 (wt%)	0.77	0.02	1.96	0.07	0.13	0.01	0.21	0.01	0.13	0.00	2.65	0.10	2.24	0.08
Al_2O_3 (wt%)	18.04	2.23	14.66	0.76	12.16	0.92	13.25	0.90	13.09	0.58	13.37	0.67	13.53	0.55
MgO (wt%)	11.10	0.86	7.38	0.37	0.05	0.01	0.14	0.01	0.09	0.01	7.17	0.38	3.47	0.20
FeO (wt%)	8.36	0.83	10.97	0.49	1.55	0.08	1.47	0.07	1.05	0.02	11.12	0.47	12.24	0.48
MnO (wt%)	0.15	0.00	0.20	0.01	0.04	0.00	0.04	0.00	0.05	0.00	0.17	0.01	0.19	0.01
CaO (wt%)	12.23	0.84	10.92	0.56	0.61	0.04	0.57	0.04	0.51	0.03	11.57	0.52	7.04	0.32
Na_2O (wt%)	2.06	0.10	2.65	0.13	4.50	0.24	4.37	0.19	4.31	0.16	2.20	0.17	3.15	0.17
K_2O (wt%)	0.02	0.00	0.14	0.01	4.27	0.15	5.16	0.25	4.77	0.08	0.50	0.03	1.75	0.09
P_2O_5 (wt%)	0.05	0.00	0.22	0.02	0.01	0.00	0.03	0.00	0.01	0.00	0.27	0.02	0.36	0.02
Sc (ppm)	31.0	0.7	40.4	2.9	3.6	0.3	3.8	0.2	3.9	0.1	30.8	1.4	32.6	1.5
V (ppm)	201	7	338	23	2	0	3	0	1	0	309	14	413	20
Cr (ppm)	407	59	244	19	0.4	0.1	0.5	0.2	2.7	3.7	291	14	15	2
Co (ppm)	48	2	42	3	0	0	1	0	0	0	44	2	37	2
Ni (ppm)	167	9	87	7	0	0	0	0	0	0	117	6	12	1
Cu (ppm)	96	6	64	3	2	0	6	0	6	0	128	7	19	2
Zn (ppm)	50	6	84	12	71	5	38	2	44	3	89	7	123	9
Ga (ppm)	15	1	19	1	21	1	18	1	17	1	21	1	22	1
Ge (ppm)	1.3	0.1	1.5	0.1	1.7	0.2	1.7	0.1	1.7	0.1	1.5	0.1	1.5	0.1
Y (ppm)	18	1	45	5	2	0	2	0	2	0	24	2	34	2
Zr (ppm)	34	2	141	14	46	3	38	2	38	2	160	12	181	11
S (^{32}S) (ppm)	939	56	1322	96	202	13	244	11	134	6	94	62	159	127
S (^{34}S) (ppm)	958	50	1319	99	102	23	69	13	59	9	96	63	159	126

is 10 ppm for ^{32}S and 20 ppm for ^{34}S, low enough to analyze most geological materials. External precision is controlled by instabilities in the instrument, laser ablation system, and natural heterogeneity. External RSD values decrease from ~25 % for samples with <100 ppm S to <10 % for samples with >1000 ppm S (Fig. 5). For high concentration samples, external reproducibilities are not as good as those reported for electron microprobe analysis (< 5 %), but for low concentrations, external reproducibilities are comparable or better than electron microprobe analysis (10–50 %) as can be seen by comparing Tables 1 and 2.

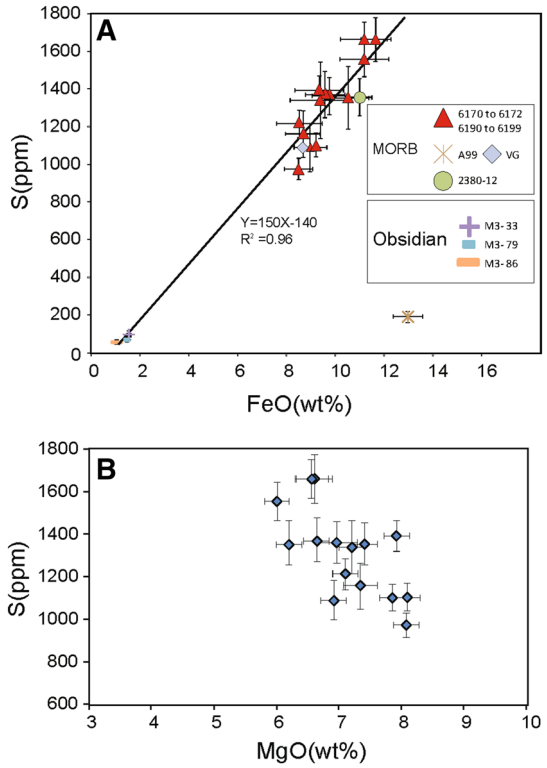

Fig. 6 Volcanic glasses. **a** Plot of S (ppm) versus FeO_{total} (wt%) in various glasses. Each point represents the mean value of several repeat measurements. *Error bars* represent external reproducibilities (1 SD). **b** S concentration versus MgO (wt%) versus S in MORB glasses

We used MORB glass VG2 for external calibration. We adopted a value of 1378 ppm, representing the average of literature-compiled data in Table 1. MORB glass A99 was not used for calibrations because of the need for large extrapolations when analyzing high S content materials. Literature compiled values of S for A99 range between 96 and 200 ppm. Calibrated against 1378 ppm S in VG2, our measurements give a value of 187 ± 29 ppm for A99.

5.2 Sulfur in rhyolite and MORB glasses

Sulfur concentrations in 3 rhyolite and 17 MORB glasses are shown in Fig. 6 and Table 2. The rhyolite glasses have 58–94 ppm S while the MORB glasses have 960–1660 ppm except for sample A99. External reproducibilities for the rhyolites are 16–22 % (1 RSD). Most MORB glasses show less than 10 % external RSD although some show RSDs as low as 3 %. Higher RSDs of 16 % may thus reflect sample heterogeneity.

In Fig. 6a, we plot S contents of rhyolites and MORBs against total FeO content determined by laser ablation. It can be seen that most samples, including the rhyolites, define a positive correlation between S and FeO. A few samples, such as MORB A99 as well as Hawaiian basalt BHVO-2g, fall well below the array. The positive correlation is consistent with the fact that S solubility at sulfide saturation correlates with total FeO content because Fe-sulfide complexes

Fig. 7 S and Cu contents in an aphyric vesiculated alkali basalt from the Sierra Nevada, California (USA). **a**, **b** represent spatial variation of S as a function of distance along the transects. Locations of *bubbles* are denoted. **c**, **d** show S versus Cu and FeO_{total}. Lack of correlation indicates that Cu remains unaffected by S degassing

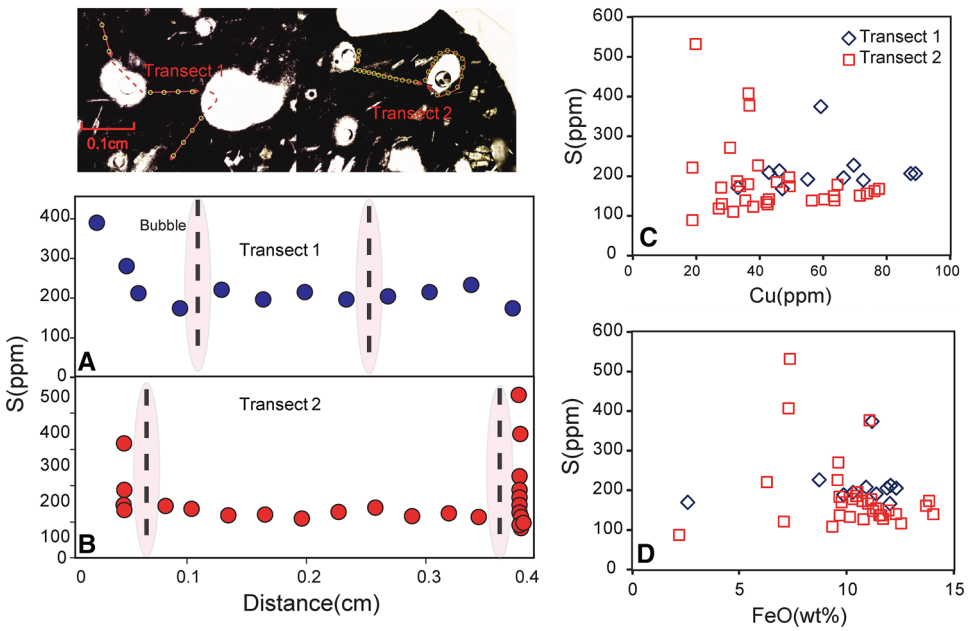

Table 3 Aphyric vesiculated basalt

	Transect 1											Transect 2								
	DY1-1	DY1-2	DY1-3	DY1-4	DY1-5	DY1-6	DY1-7	DY1-8	DY1-9	DY1-10	DY1-11	DY2-1	DY2-2	DY2-3	DY2-4	DY2-5	DY2-6	DY2-7	DY2-8	DY2-9
SiO_2 (wt%)	46.28	50.66	50.13	49.62	51.33	50.00	50.73	51.86	51.61	52.09	53.49	52.47	54.30	51.36	52.92	52.64	51.34	51.94	53.16	51.57
TiO_2 (wt%)	1.64	2.04	1.65	1.78	1.75	1.52	1.90	2.00	2.09	1.87	0.55	1.73	1.88	2.72	1.30	1.97	2.26	2.37	1.93	1.86
Al_2O_3 (wt%)	17.96	14.66	14.46	14.58	16.98	14.93	14.97	15.81	13.93	17.29	25.62	17.23	16.87	14.19	11.90	16.33	13.31	14.72	15.29	15.19
MgO (wt%)	4.75	4.57	6.64	6.00	4.03	6.06	4.95	3.64	4.62	3.23	0.79	4.97	3.87	5.37	8.60	4.32	6.87	5.48	4.96	6.33
FeO (wt%)	11.19	12.32	12.02	12.06	9.86	10.91	11.39	10.30	11.89	8.72	2.57	9.57	9.67	13.86	11.07	11.15	13.72	12.31	11.24	11.53
MnO (wt%)	0.18	0.18	0.18	0.18	0.15	0.18	0.18	0.16	0.19	0.14	0.03	0.16	0.15	0.20	0.18	0.17	0.21	0.20	0.18	0.18
CaO (wt%)	10.63	8.39	8.48	9.65	9.28	9.48	9.52	9.59	9.21	9.37	11.68	10.61	9.30	8.67	9.33	9.55	8.92	9.38	9.61	9.89
Na_2O (wt%)	4.69	4.17	3.66	3.53	3.80	4.32	3.53	3.75	3.42	4.37	3.16	3.58	4.05	3.60	5.19	3.94	3.53	3.86	3.72	3.69
K_2O (wt%)	0.71	0.84	0.69	0.58	0.69	0.58	0.67	0.73	0.81	0.71	0.20	0.54	0.72	0.80	0.57	0.74	0.72	0.59	0.72	0.64
P_2O_5 (wt%)	0.19	0.34	0.30	0.23	0.31	0.26	0.34	0.33	0.40	0.37	0.07	0.32	0.36	0.42	0.20	0.35	0.36	0.34	0.38	0.32
Sc (ppm)	25	24	26	32	25	26	30	30	27	25	4	34	26	34	33	31	37	32	30	33
V (ppm)	190	205	188	228	205	186	200	225	209	194	51	208	219	293	163	224	277	234	220	207
Cr (ppm)	125	74	133	121	224	136	122	104	95	87	8	144	129	98	164	75	135	91	137	156
Co (ppm)	36	40	47	44	29	41	39	29	38	25	7	30	28	41	46	32	46	38	36	40
Ni (ppm)	34	39	60	46	25	54	36	20	34	19	5	28	25	37	62	26	51	36	33	42
Cu (ppm)	59	87	47	46	73	43	55	66	89	70	33	39	45	49	37	64	76	43	63	63
Zn (ppm)	52	102	93	91	91	96	98	94	114	89	27	86	99	127	82	115	128	103	109	101
Ga (ppm)	27	24	21	21	23	25	22	25	25	24	22	25	25	24	15	25	21	24	23	23
Ge (ppm)	1.6	1.5	1.5	1.5	1.4	2.0	1.6	1.5	1.5	1.6	1.0	1.2	1.7	1.6	1.4	1.8	1.6	1.8	1.6	1.5
Y (ppm)	25	30	22	19	24	20	28	27	33	27	5	25	28	34	20	30	29	26	30	26
Zr (ppm)	125	155	118	95	122	95	142	134	170	142	25	125	143	180	122	150	149	133	151	135
S (^{32}S) (ppm)	373	205	166	211	188	207	190	194	204	226	169	225	183	173	376	176	160	139	147	137
S (^{34}S) (ppm)	383	215	181	221	182	204	178	185	208	227	135	231	196	166	382	170	165	142	148	143

	Transect 2										
	DY2-10	DY2-11	DY2-12	DY2-13	DY2-14	DY2-15	DY2-16	DY2-17	DY2-18	DY2-19	DY2-20
SiO_2 (wt%)	53.02	54.32	52.63	52.49	51.64	57.58	54.49	51.75	52.77	52.05	53.03
TiO_2 (wt%)	2.06	2.08	1.80	1.93	1.92	1.02	1.64	2.23	1.55	1.66	1.87
Al_2O_3 (wt%)	15.93	14.64	16.91	15.05	12.16	11.89	16.08	16.00	16.04	14.95	16.73
MgO (wt%)	4.51	4.12	4.61	5.72	8.17	6.08	4.36	5.11	6.01	6.91	4.22
FeO (wt%)	11.37	11.01	9.67	11.96	14.06	7.34	7.28	10.28	9.61	10.45	10.15

Table 3 continued

	Transect 2										
	DY2-10	DY2-11	DY2-12	DY2-13	DY2-14	DY2-15	DY2-16	DY2-17	DY2-18	DY2-19	DY2-20
MnO (wt%)	0.17	0.18	0.15	0.19	0.23	0.12	0.11	0.17	0.15	0.18	0.16
CaO (wt%)	9.10	9.57	10.50	9.05	8.89	9.32	10.03	10.21	9.29	10.23	9.73
Na_2O (wt%)	3.92	3.95	4.03	3.81	3.19	7.15	6.29	4.40	4.93	4.07	4.14
K_2O (wt%)	0.74	0.86	0.58	0.64	0.64	0.60	0.65	0.68	0.59	0.49	0.75
P_2O_5 (wt%)	0.37	0.44	0.30	0.36	0.37	0.14	0.23	0.34	0.25	0.24	0.39
Sc (ppm)	28	34	31	28	36	25	27	34	28	38	30
V (ppm)	226	260	238	200	224	147	186	218	162	220	220
Cr (ppm)	101	116	532	106	182	320	80	132	94	213	120
Co (ppm)	33	30	30	41	55	26	20	31	32	37	29
Ni (ppm)	28	22	28	42	65	29	16	34	32	42	24
Cu (ppm)	74	77	56	71	60	20	36	36	31	33	42
Zn (ppm)	112	118	90	118	124	41	50	85	70	77	102
Ga (ppm)	23	26	24	24	20	14	18	22	19	19	25
Ge (ppm)	1.6	1.7	1.6	1.6	1.8	1.3	1.4	1.4	1.4	1.6	1.8
Y (ppm)	29	34	23	27	28	13	22	30	21	22	29
Zr (ppm)	151	166	116	137	141	113	141	155	126	108	148
S (^{32}S) (ppm)	154	166	136	149	139	531	406	178	269	185	132
S (^{34}S) (ppm)	151	171	148	159	137	544	413	189	273	189	132

	Transect 2								
	DY2-21	DY2-22	DY2-23	DY2-24	DY2-25	DY2-26	DY2-27	DY2-28	DY2-29
SiO_2 (wt%)	53.38	51.38	51.69	53.66	52.41	53.07	51.24	52.11	51.12
TiO_2 (wt%)	1.97	1.91	1.71	1.22	1.98	1.33	2.68	1.65	1.90
Al_2O_3 (wt%)	15.58	20.01	14.09	18.56	14.28	21.18	16.70	16.79	15.66
MgO (wt%)	4.82	3.30	7.40	4.34	6.26	2.78	4.34	5.85	6.44
FeO (wt%)	10.79	9.33	12.55	6.27	10.73	7.06	11.61	9.76	11.70
MnO (wt%)	0.17	0.13	0.20	0.11	0.17	0.11	0.16	0.15	0.18
CaO (wt%)	9.56	10.22	9.36	11.13	10.32	11.03	9.45	9.85	9.95
Na_2O (wt%)	3.79	4.11	3.49	5.28	4.21	3.86	4.04	4.27	3.43
K_2O	0.73	0.46	0.46	0.41	0.53	0.44	0.57	0.51	0.52
P_2O_5 (wt%)	0.40	0.28	0.30	0.18	0.32	0.27	0.35	0.26	0.30
Sc (ppm)	31	19	32	27	37	17	29	28	32
V (ppm)	240	196	220	150	243	137	282	198	222
Cr (ppm)	145	40	162	122	196	43	69	87	149

Table 3 continued

	Transect 2								
	DY2-21	DY2-22	DY2-23	DY2-24	DY2-25	DY2-26	DY2-27	DY2-28	DY2-29
Co (ppm)	33	27	47	20	36	20	33	34	42
Ni (ppm)	29	22	56	20	37	18	26	39	47
Cu (ppm)	42	32	27	19	34	38	35	28	28
Zn (ppm)	113	92	101	43	91	71	112	79	97
Ga (ppm)	24	26	21	21	21	24	25	22	21
Ge (ppm)	1.6	1.5	1.8	1.4	1.6	1.4	1.6	1.4	1.5
Y (ppm)	28	18	22	15	26	18	26	20	22
Zr (ppm)	143	103	109	87	133	92	142	110	110
S (^{32}S) (ppm)	126	108	116	220	173	121	136	169	128
S (^{34}S) (ppm)	139	113	113	210	182	108	131	183	140

increase S solubility in the melt (Mavrogenes and O'Neill 1999; Perfit et al. 1983). The variation in FeO is due to crystal-liquid fractionation, indicating that MORBs are sulfide-saturated or quickly become sulfide-saturated soon after leaving their mantle source regions and differentiating. Those samples with anomalously low S for a given FeO content likely lost S by degassing.

5.3 Sulfur in aphyric groundmass of basaltic lavas

Although laser ablation holds no advantage over electron probe micro-analysis in analyzing homogeneous samples, such as glasses, the ability to perform in situ bulk sampling by laser ablation may be useful when the S content of aphyric groundmass in lavas is desired. The amount of S remaining in erupted lavas or shallowly intruded magmas is often used to quantify how much S has degassed during emplacement (Self et al. 2008), provided some estimate of undegassed S content is known (this is usually taken as the S content at sulfide saturation). To date, most S measurements are done by whole-rock analyses, but lava flows are commonly subjected to weathering and alteration, especially in highly vesiculated samples. These post-emplacement processes could lead to addition or leaching of S. *In situ* methods may allow one to quantify S in small areas of the rock that have not been altered. To explore this, we analyzed S in a vesiculated basalt with an aphyric groundmass, consisting of microlites and microphenocrysts less than 30 μm in diameter.

In Fig. 7 and Table 3 we show two line traverses across a basalt thin section (DY1, an ultrapotassic lava flow from the Owens Valley, California). The traverses were designed to explore how S varies with distance from high permeability areas, such as the vesicles. S contents are mostly around 200 ppm, indicating that at least 80 % of the S has degassed. We note that concentrations as high as 400 ppm are found near vesicle walls. This could imply that external S has been added to the basalt via the vesicles. Alternatively, the S on vesicle walls could represent a fraction of the S degassed into the vesicles, but a more dedicated study is necessary to evaluate this possibility. For completeness, we show that Cu, simultaneously analyzed with S, does not correlate with S. Cu is strongly controlled by the presence of sulfide, so the lack of correlation suggests that any sulfides present have already broken down (resulting in volatile loss of S) or most of the S was originally dissolved in the silicate magma, but was lost by degassing.

5.4 Micro-laminated sediments

Another application of this method is the fine-scale elemental mapping of micro-laminated sediments. We examined an organic rich marl from the mid-Cretaceous

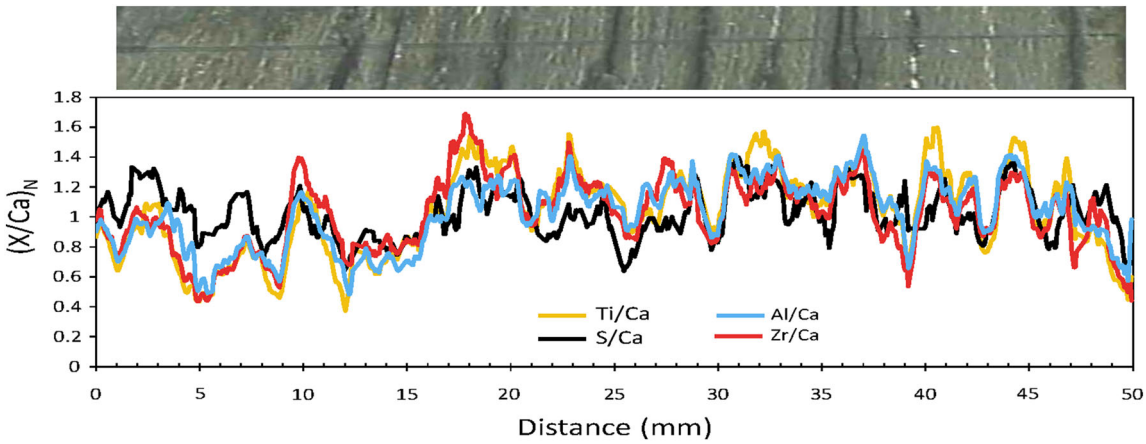

Fig. 8 Elemental composition of micro-laminated Cretaceous Eagleford Formation limestones. Ca-normalized elemental profiles versus distance across a micro-laminated organic rich limestone from the Cretaceous Eagleford Formation in Lozier Canyon, Texas. Data represent 15 point running averages. Normalization to Ca was done to eliminate the dilution/concentration effects of changes in material density due to variations in porosity or crack density. Data are in units of wt% metal divided by w% Ca metal

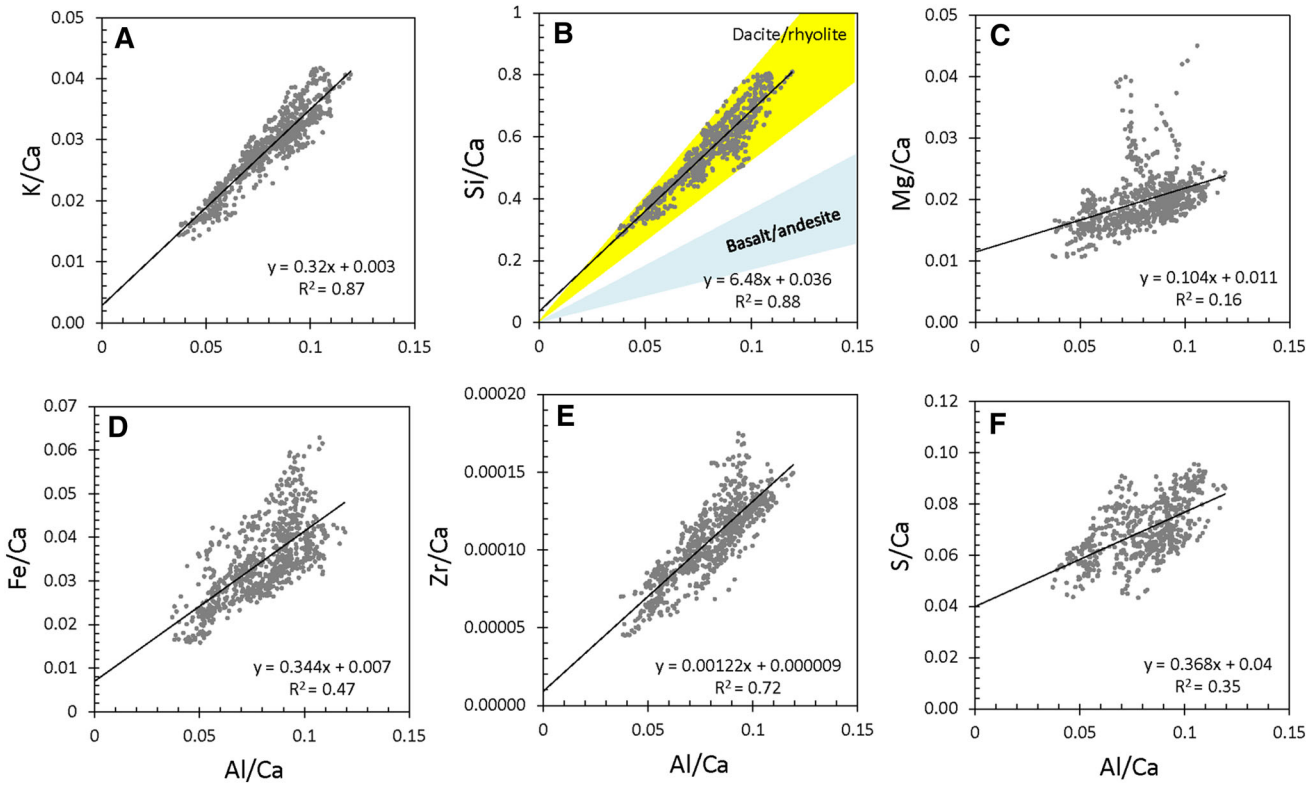

Fig. 9 Elemental composition of micro-laminated Cretaceous Eagleford Formation limestones. Same analyses as in Fig. 8, but individual running averages for different elements are plotted against each to evaluate correlations. All data re normalized to Ca. X-axis in all *panels* corresponds to Al/Ca (wt%/wt% by metal). **a** K/Ca. **b** Si/Ca. **c** Mg/Ca. **d** Fe/Ca. **e** Zr/Ca. **f** S/Ca. In **b**, range of Si/Al ratios (by weight) for dacite/rhyolite and basalt/andesite are shown for reference

Eagleford Shale (near the Cenomanian-Turonian boundary), sampled by Lee from the Lozier Canyon section in Terrell County, Texas. This marl is intercalated by numerous discrete volcanic ash layers associated with mid-Cretaceous magmatic flareup in the Sierra Nevada batholith towards the west (Lee et al. 2013). The ash layers are nearly always recessive whereas the marls tend to form resistant layers. Our objective was to examine the finely laminated marl layers to quantify whether such layers also contain ash. This was done by performing a continuous real

Table 4 Synthetic amber glasses

N	Bud light		Saint Arnold's		Bullseyeglass 001322-0003-F-P001		Bullseyeglass 000203-0003-F-P005	
	23		27		6		7	
	Average wt%	1 SD	Average wt%	1 SD	Average wt%	1 SD	Average wt%	1 SD
SiO_2	70.61	0.97	70.45	0.75	71.50	0.89	71.93	0.53
TiO_2	0.03	0.03	0.08	0.00	0.02	0.00	0.04	0.00
Al_2O_3	1.3	0.03	1.32	0.05	2.22	0.09	5.98	0.14
MgO	0.27	0.01	0.37	0.01	2.52	0.07	0.05	0.00
FeO_T	0.49	0.02	0.41	0.01	0.04	0.00	0.05	0.00
MnO	0.02	0.00	0.01	0.00	0.00	0.00	0.00	0.00
CaO	11.94	0.24	11.66	0.3	4.06	0.14	5.03	0.24
Na_2O	12.62	0.39	12.52	0.28	18.20	0.83	14.80	0.20
K_2O	0.63	0.02	0.25	0.01	0.55	0.03	1.18	0.03
P_2O_5	0.01	0.00	0.02	0.00	0.03	0.00	0.01	0.00
Total	97.93	0.78	97.5	0.8	99.13	2.05	99.07	1.15
	ppm		ppm		ppm		ppm	
S (^{32}S)	314	41	296	24	296	16	728	63
S (^{34}S)	318	38	299	41	286	22	726	58

time 50 mm long line transect with a 110 μm laser spot size (10 Hz repetition rate and 10 J/cm^2 power) at a velocity of 15 μm/s. Signal intensities were converted to concentrations using methods outlined above (see also Lee et al. 2009). To correct for concentration/dilution effects associated with variations in sample density (caused by variations in porosity and crack density), all elements were normalized to Ca. Select elemental transects are shown in Fig. 8, where we have also normalized to the long-term average so that all elemental ratios can be plotted on the same scale. To reduce some of the inherent instability of the measurements, a 15 point running average was applied. Variations in the marl and detrital components can be seen in the variations of Al/Ca ratio among other elemental ratios. Figure 9, shows individual data points (15 point running average) of elements normalized to Ca. It can be seen that K, Al, and Si are highly correlated and their regression parameters intersect zero to within error. Such behavior indicates that the marls represent simple mixtures between pure limestone and a detrital component. In contrast, even though Mg/Ca and Al/Ca are well correlated, there is a non-zero Mg/Ca intercept, indicating that the pure limestone contains a small amount of Mg. More surprising is the correlation of Fe/Ca and Zr/Ca versus Al/Ca. These elements, especially Zr, are not expected to be enriched in clays. Zr is more likely associated with volcanic ash or zircons, but the lack of Zr spikes in the transect suggest that such Zr is not related to the presence of zircon grains. We note that the Si/Al ratio (Fig. 9b) defined by our data matches that of dacites/rhyolites rather than basalts and andesites and/or pure clay components, providing additional support for an ash component even in the finely laminated marls. It is in this context where our S measurements may be interesting. In Fig. 9f, it can be seen that S/Ca is weakly correlated with Al/Ca (and by inference with K, Si, Zrand Fe as well). We do not know how to interpret this preliminary data, but such a correlation at first seems surprising because volcanic ash (or any detrital component), which consists of silicates and oxides primarily, is not expected to have much S. We thus interpret the S-Al correlation as possible evidence that precipitation of S, in the form of sulfide in these organic C rich marls, must be enhanced in the presence of volcanic ash, which may serve as a nutrient (Censi et al. 2010; Lee et al. 2013). More work is necessary to explore the significance of this correlation, but this study highlights the potential for using laser ablation to S microstratigraphy.

5.5 Amber glasses as in-house standards

Finally, towards developing a homogeneous in house standard of sufficient quantity, we have turned to industrial amber glasses. Sulfate is used in the fining process of making glass and reduced S is important for making the dark color of amber glasses through the formation of Fe^{3+}-S^{2-} chromophores (Albayrak and Sengel 2008). We have chosen amber beer glass from Anheuser-Busch's Bud Light™ (Jones and Brossia 2006) and Saint Arnold's™

beer and S-bearing glasses (001322-0003-F-P001 and 000203-0003-F-P005) used for decorative glass arts (Bullseyeglass.com). Random fragments of these glasses were analyzed to assess homogeneity and S concentrations (Table 4). The glasses range from ~300 to 700 ppm S. Bullseye^{TM} glass P001 has the lowest RSD deviation of 5 % for ^{32}S, followed by Bullseye^{TM} glass P005 at 9 % RSD, St. Arnold's^{TM} at 8 % and Bud Light^{TM} at 13 %.

6 Conclusions

Sulfur measurement by LA-ICPMS is established here with a longtime reproducibility for homogenous samples of 10 % for high concentration samples (>900 ppm) and ~20 % for low concentration (<200 ppm) samples. The primary challenge is correcting for long-term instrumental drift in elemental fractionation factors. This method is shown here to be applicable to rapid in situ characterization of S in glass, aphyric groundmass of volcanic rocks, and micro-laminated sediments.

Acknowledgments This work was supported by NSF OCE-1338842. The contents in the amber beer bottles were quantitatively decanted into a kitchen sink to prevent unintentional (or intentional) consumption by human subjects. Monica Erdman, Michael Farner, and Xun Yu are thanked for discussions and help in the laboratory.

References

Albayrak G, Sengel H (2008) Review of sulphate chemistry and its impact on glass production. Eur J Glass Sci Technol 49:289–296

Alt JC (1995) Sulfur isotopic profile through the oceanic crust: sulfur mobility and seawater-crustal sulfur exchange during hydrothermal alteration. Geology 23:585–588

Alt JC, Shanks WCI, Jackson MC (1993) Cycling of sulfur in subduction zones: the geochemistry of sulfur in the Mariana Island arc and back-arc trough. Earth Planet Sci Lett 119:477–494

Alt JC, Garrido CJ, Shanks WCI, Turchyn AV, Padron-Navarta JA, Sanchez-Vizcaino VL, Pugnaire MTG, Marchesi C (2012) Recycling of water, carbon, and sulfur during subduction of serpentinites: a stable isotope study of Cerro del Almirez, Spain. Earth Planet Sci Lett 327–328:50–60

Bell AS, Simon A, Guillong M (2009) Experimental constraints on Pt, Pd, and Au partitioning and fractionation in silicate melt-sulfide-oxide-aqueous fluid systems at 800 ^{O}C, 150 MPa and variable sulfur fugacity. Geochim Cosmochim Acta 73:5778–5792

Burgisser A, Scaillet B (2007) Redox evolution of a degassing magma rising to the surface. Nature 445:194–197

Censi P, Randazzo LA, Zuddas P, Saiano F, Arico P, Ando S (2010) Trace element behaviour in seawater during Etna's pyroclastic activity in 2001: concurrent effects of nutrients and formation of alteration minerals. J Volcanol Geotherm Res 193:106–116

De Hoog JCM, Mason PRD, Van Bergen MJ (2001) Sulfur and chalcophile elements in subduction zones: constraints from a laser ablation ICP-MS study of melt inclusions from Galunggung volcano, Indonesia. Geochim Cosmochim Acta 65:3147–3164

de Hoog JCM, Hattori KH, Hoblitt RP (2004) Oxidized sulfur-rich mafic magma at Mount Pinatubo, Philippines. Contrib Mineral Petrol 146:750–761

Dixon JE, Clague DA, Stolper EM (1991) Degassing history of water, sulfur, and carbon in submarine lavas from Kilauea Volcano, Hawaii. J Geol 99:371–394

Erdman ME, Lee C-TA, Yang W, Ingram L (2013) Sulfur concentration in geochemical reference materials by solution ICP–MS. Geostand Geoanal Res 38:51–60

Gao S, Liu X, Yuan H, Hattendorf B, Günther D, Chen L, Hu S (2002) Determination of forty two major and trace elements in USGS and NIST SRM glasses by laser ablation-inductively coupled plasma-mass spectrometery. Geostand Newsl 26:181–196

Jarosewich EJ, Nelen JA, Norberg JA (1979) Reference samples for electron microprobe analysis. Geostand Newsl 4:43–47

Jego S, Dasgupta R (2013) Fluid-present melting of sulfide-bearing ocean-crust: experimental constraints on the transport of sulfur from subducting slab to mantle wedge. Geochem Cosmochim Acta 110:106–134

Jones S, Brossia CE (2006) Method for the production of amber glass with reduced sulfur-containing emissions, United States Patent Application Publication. Anheuser-Busch Inc, United States of America

Jugo PJ (2009) Sulfur content at sulfide saturation in oxidized magmas. Geology 37:415–418

Lee C-A, Oka M, Luffi P, Agranier A (2008) Internal distribution of Li and B in serpentinites from the Feather River Ophiolite, California, based on laser ablation inductively coupled plasma mass spectrometry. Geochem Geophys Geosyst 9. doi:10.1029/2008GC002078

Lee C-TA, Oka M, Luffi P, Agranier A (2009) Internal distribution of Li and B in serpentinites from the Feather River Ophiolite, California based on laser ablation inductively coupled plasma mass spectrometry. Geochem Geophys Geosyst 9. doi:10.1029/2008GC002078

Lee C-TA, Luffi P, Chin EJ, Bouchet R, Dasgupta R, Morton DM, Le Roux V, Yin Q-Z, Jin D (2012) Copper systematics in arc magmas and implications for crust-mantle differentiation. Science 336:64–68

Lee C-TA, Shen B, Slotnick BS, Liao K, Dickens GR, Yokoyama Y, Lenardic A, Dasgupta R, Jellinek M, Lackey JS, Schneider T, Tice M (2013) Continental arc-island arc fluctuations, growth of crustal carbonates and long-term climate change. Geosphere 9:21–36

Liu Y, Hu Z, Gao S, Günther D, Xu J, Gao C, Chen H (2008) In situ analysis of major and trace elements of anhydrous minerals by LA-ICP-MS without applying an internal standard. Chem Geol 257:34–43

Longerich HP, Jackson SE, Gunther D (1996) Laser ablation inductively coupled plasma mass spectrometric transient signal data acquisition and analyte concentration calculation. J Anal Atomic Spectrom 11:899–904

Mavrogenes JA, O'Neill HSC (1999) The relative effect of pressure, temperature and oxygen fugacity on the solubility of sulphide in mafic magmas. Geochim Cosmochim Acta 63:1173–1180

Melson WG, O'Hearn T, Jarosewich E (2002) A data brief on the Smithsonian Abyssal Volcanic Glass data file. Geochem Geophys Geosys 3:1–11

Metrich N, Mandeville C (2010) Sulfur in magmas. Elements 6:81–86

Metrich N, Schiano P, Clocchiatti R, Maury RC (1999) Transfer of sulfur in subduction settings: an example from Batan Island (Luzon volcanic arc, Philippines). Earth Planet Sci Lett 167:1–14

Nilsson K, Peach CL (1993) Sulfur speciation, oxidation state, and sulfur concentration in back arc magmas. Geochim Cosmochim Acta 57:3807–3813

O'Neill HSC, Mavrogenes JA (2002) The sulfide capacity and the sulfur content at sulfide saturation of silicate melts at 1400 & #xB0;C and 1 bar. J Petrol 43:1049–1087

Perfit MR, Fornari DJ, Malahoff A, Embley RW (1983) Geochemical studies of abyssal lavas recovered by DSRV Alvin from eastern Galapagos Rift, Inca Transform, and Ecuador Rift 3. Trace element abundances and petrogenesis. J Geophys Res 88: 10551–10572

Ripley EM, Li C, Moore CH, Elswick ER, Maynard JB, Paul RL, Sylvester P, Seo JH, Shimizu N (2011) Analytical methods for sulfur determination in glasses, rocks, minerals and fluid inclusions. Rev Mineral Geochem 73:9–39

Savov IP, Leeman WP, Lee C-TA, Shirey SB (2009) Boron isotopic variations in NW USA rhyolites: Yellowstone, Snake River Plain, Eastern Oregon. J Volcanol Geotherm Res 188:162–172

Self S, Blake S, Sharma K, Widdowson M, Sephton S (2008) Sulfur and chlorine in late Cretaceous Deccan magmas and eruptive gas release. Science 319:1654–1657

Thordarson T, Self S, Oskarsson N, Hulsebosch T (1996) Sulfur, chlorine, and fluorine degassing and atmospheric loading by the 1783–1784 AD Laki (Skaftar Fires) eruption in Iceland. Bull Volcanol 58:205–225

Thornber CR, Sherrod DR, Siems DF, Heliker CC, Meeker GP, Oscarson RL, Kauahikaua JP (2002) Whole-rock and glass major-element geochemistry of Kilauea Volcano, Hawaii, Near-vent eruptive products, September 1994 through September 2001. US Geological Survey Open File Report OF02-17

Wallace PJ (2005) Volatiles in subduction zone magmas: concentrations and fluxes based on melt inclusion and volcanic gas data. J Volcanol Geotherm Res 140:217–240

Wallace PJ, Carmichael ISE (1992) Sulfur in basaltic magmas. Geochem Cosmochim Acta 56:1863–1874

Wallace PJ, Edmonds M (2011) The sulfur budget in magmas: evidence from melt inclusions, submarine glasses, and volcanic gas emissions. Rev Minerol Geochem 73:215–246